View metadata, citation and similar papers at core.ac.uk

brought to you by CORE

provided by Kyoto University Research Information Repository

KURENAI
Kyoto University Research Information Repository

KYOTO UNIVERSITY

Title	Coupled thermo-hydro-mechanical-chemical modeling by incorporating pressure solution for estimating the evolution of rock permeability
Author(s)	Yasuhara, Hideaki; Kinoshita, Naoki; Ogata, Sho; Cheon, Dae Sung; Kishida, Kiyoshi
Citation	International Journal of Rock Mechanics and Mining Sciences (2016), 86: 104-114
Issue Date	2016-07-01
URL	http://hdl.handle.net/2433/217409
Right	© 2016. This manuscript version is made available under the CC-BY-NC-ND 4.0 license http://creativecommons.org/licenses/by-nc-nd/4.0/; The full-text file will be made open to the public on 01 July 2018 in accordance with publisher's 'Terms and Conditions for Self-Archiving'.; This is not the published version. Please cite only the published version. この論文は出版社版でありません。引用の際には出版社版をご確認ご利用ください。
Type	Journal Article
Textversion	author

Kyoto University

Coupled thermo-hydro-mechanical-chemical modeling of permeability change in porous rocks: The significant role of the pressure solution

Hideaki Yasuhara[1], Naoki Kinoshita[1], Sho Ogata[1], Dae-Sung Cheon[2], and Kiyoshi Kishida[3]

[1] Department of Civil and Environmental Engineering, Ehime University, Matsuyama, 790-8577, JAPAN.

[2] Korea Institute of Geoscience and Mineral Resources, Daejeon, 305-350, KOREA.

[3] Department of Urban Management, Kyoto University, Kyoto, 615-8540, JAPAN.

*Corresponding Author, hide@cee.ehime-u.ac.jp; Tel&Fax: +81-89-927-9853

Abstract

When considering the safe isolation of high-level radioactive wastes, the long-term evolution of the hydraulic and transport behavior of the rocks of interest should be predicted prior to its operation because coupled thermal-hydraulic-mechanical-chemical (THMC) processes should be significantly active in such situations where relatively high ground pressure and temperature are induced. In this study, a coupled THMC numerical model has been developed to examine the long-term change in permeability of the porous sedimentary rocks that are assumed to be composed purely of quartz. Specifically, the chemo-mechanical process of the pressure solution was incorporated into the model. The developed model was validated by replicating the existing experimental measurements of the porosity reduction and the evolving silica concentration. Subsequently, by simulating the burial of high-level radioactive wastes in the deep subsurface, namely, by applying the simulated confining pressure and temperature conditions, the long-term evolution of the rock permeability was predicted. The model predictions clearly showed a significant influence of the pressure dissolution on the change in permeability with time. The predicted permeability of the rocks close to the wastes decreased by one order of magnitude in 10^4 years when considering the pressure dissolution, while the permeability changed little during the same period when the pressure dissolution was not considered. This reduction should delay the dispersion of the radioactive materials dissolved in the groundwater.

Keywords: Rock permeability, Coupled THMC model, Mineral dissolution, Pressure solution

Highlights:

- **A coupled THMC numerical model was developed to predict the long-term change in permeability.**
- **The developed model considers the pressure solution.**
- **The model was validated by replicating the existing experiments.**
- **The model enables the long-term evolution of rock permeability to be predicted under arbitrary pressure and temperature conditions.**

1. Introduction

When disposing high-level radioactive wastes in the deep subsurface, the influence of the disposal on the hydraulic property of the rocks of interest must be examined in advance and should be estimated with a certain level of precision. The rocks that work as natural barriers to the

46 migration of radionuclides should be influenced by the convolved phenomena, including the
47 transfer of heat from the wastes, the groundwater flow, the variation in induced stresses, and the
48 geochemical reactions, such as mineral dissolution and precipitation [1], [2]. Therefore, in order
49 to predict the long-term evolution of the hydraulic property, a numerical model that can account
50 for the coupled Thermo-Hydro-Mechanical-Chemical (THMC) processes is required. In particular,
51 the precise modeling of the geochemical reactions, occurring at the interface between the grain
52 particles composing the rocks and the pore water, is of significant importance to achieving precise
53 predictions. To date, THMC numerical models have been developed to address such engineering
54 issues as the geological isolation of CO_2 and radioactive wastes and energy recovery from
55 geothermal reservoirs [3]-[9]. By using some of the above models, the long-term phenomena
56 taking place in the artificial and natural barriers have been predicted by considering the specific
57 geological conditions, the heat transfer, the water flow, the stress/deformation, and the
58 geochemical reactions. In the geochemical calculations of the THMC models, the mineral
59 dissolution and precipitation occurring on the free surfaces of the rocks [10] are typically
60 considered, but the dissolution active at the grain contacts (e.g., pressure dissolution [11]-[18]) is
61 not taken into account. In the literature, it is indicated that the pressure dissolution may change the
62 hydraulic property over a long duration; and therefore, the phenomenon must be incorporated into
63 the modeling process when evaluating the long-term integrity of the rocks in terms of the

64 hydraulic property. Recently, several THMC numerical models that can consider the process of
65 the pressure dissolution have been proposed [7]-[9], but these models mostly address fracture
66 media and do not estimate the evolution of the hydraulic property in porous rocks.

67 In this study, a new coupled THMC numerical model that incorporates the important process
68 of the pressure dissolution, as well as the free-face dissolution and precipitation, was developed,
69 and the validity of the model was examined by replicating the experimental measurements
70 obtained from Elias and Hajash (1992) [19]. Subsequently, the long-term evolution of the
71 permeability in porous rock was predicted under the expected stress and temperature conditions
72 where high-level radioactive wastes are disposed. In particular, the influence of the pressure
73 dissolution on the change in the rock permeability was examined intensively.

74 When any numerical model is developed, it may be dilemmatic to consider the balance
75 between the simplicity and the precision of the model. Complex models that incorporate a number
76 of equations to be solved may require time-consuming handling during pre- and post-processing,
77 and lengthy calculation time. Therefore, simpler or more straightforward numerical models with
78 satisfactory precision are preferred for general users. By focusing selectively on the geochemical
79 process of the pressure dissolution, the minor objective of this study is to develop a relatively
80 simple model.

81

2. Model description

The coupled THMC model developed in this work enables the change in permeability of porous rocks to be followed with time by considering the interactions of the thermal, hydraulic, mechanical, and geochemical processes (i.e., heat transfer, groundwater flow in saturated porous media, stress/deformation, mass transport, and mineral dissolution/precipitation). The processes considered in this model are schematically summarized in **Figure 1**. As is apparent from this figure, the two-way interactions are taken into account between the T and H, the H and C, and the C and T components. In the M component, the stress distribution is calculated and then rendered to calculate a chemo-mechanical process, which is referred to as CM in **Figure 1**. In the C components, two different chemical processes are incorporated into the model; one is the free-surface dissolution/precipitation (CF) and the other is the pressure solution (CM). The pressure solution includes three serial processes - mineral dissolution at the stressed contacts, diffusive transport through the thin film of water, and re-precipitation of the mineral matter at the pore wall. The mineral dissolution at the stressed contacts is explicitly integrated into the proposed model as the CM component. It should be noted that we have proposed conceptual chemo-mechanical models to predict the change in permeability of porous and fractured rocks [20]-[24], and that this work is an attempt to fit the conceptual model into the coupled numerical

100 model and to conduct numerical simulations at a field scale instead of a representative element
101 scale. It should be also noted that the interactions between the H and M and the M ansd T
102 components are intentionally omitted in this work. These processes may influence the change in
103 permeability, but the main focus of the current work is to examine the effects of the geochemical
104 reactions (i.e., free-face dissolution/precipitation and pressure dissolution) on the change in
105 permeability by simplifying the developed model.
106
107 *2.1 Governing equations*
108 The equations used to model each of the THMC processes are presented in this section. In
109 this work, COMSOL Multiphysics [25] is utilized to solve the differential equations describing
110 the THMC processes. The calculation procedure is shown in **Figure 2** and the details are
111 described hereinafter. The coupled THMC processes are solved sequentially by exchanging the
112 dependent variables (i.e., porosity/permeability, flow velocity, stress, temperature, and
113 dissolution/precipitation rate constants).
114 The groundwater flow in saturated rocks is simply modeled by the conservation of water
115 mass and by assuming the Darcian flow, given by

$$\frac{\partial(\rho_w \phi)}{\partial t} + \nabla \cdot (\rho_w \boldsymbol{u}) = f_m , \quad (1)$$

$$\boldsymbol{u} = -\frac{\boldsymbol{k}}{\mu}(\nabla p + \rho_w g \nabla D) , \quad (2)$$

where ρ_w [kg m^{-3}] is the density of the fluid, ϕ [-] is the porosity, $\boldsymbol{u}$ [m s^{-1}] is the fluid velocity tensor, f_m [kg m^{-3} s^{-1}] is the source term for the flow, $\boldsymbol{k}$ [m^2] is the rock permeability tensor, μ [Pa s] is the fluid dynamic viscosity, p [Pa] is the fluid pressure, g [m s^{-2}] is the gravity acceleration, and D [m] is the potential head. The temperature-dependent variables of ρ_w and μ are evaluated at arbitrary temperatures within the calculation scheme [25].

The heat transfer is evaluated by considering thermal convection and conduction without the radiation effect, as follows:

$$(\rho C_p)_{eq} \frac{\partial T}{\partial t} + \rho_w C_{p,w} \boldsymbol{u} \cdot \nabla T = \nabla \cdot (\boldsymbol{k}_{eq} \nabla T) + Q_h , \quad (3)$$

where T [K] is the temperature, $(\rho C_p)_{eq}$ [J K^{-1} m^{-3}] is the equilibrium volumetric heat capacity, $C_{p,w}$ [J kg^{-1} K^{-1}] is the heat capacity of the fluid, $\boldsymbol{k}_{eq}$ [W m^{-1} K^{-1}] is the equilibrium thermal conductivity tensor, and Q_h [W m^{-3}] is the heat source. $(\rho C_p)_{eq}$ and $\boldsymbol{k}_{eq}$ can be obtained from the following equations:

$$(\rho C_p)_{eq} = (1-\phi)\rho_m C_{p,m} + \phi \rho_w C_{p,w} , \quad (4)$$

$$\boldsymbol{k}_{eq} = (1-\phi)\boldsymbol{k}_m + \phi \boldsymbol{k}_w , \quad (5)$$

where ρ_m [kg m^{-3}] is the density of the solid, $C_{p,m}$ [J kg^{-1} K^{-1}] is the heat capacity of the solid, and $\boldsymbol{k}_m$ and $\boldsymbol{k}_w$ [W m^{-1} K^{-1}] are the thermal conductivity tensors of the solid and the fluid, respectively.

The numerical model enables the temperature-dependent variables of $C_{p,m}$, $C_{p,w}$, $\boldsymbol{k_m}$, and $\boldsymbol{k_w}$ to be followed at arbitrary temperatures [25].

The mechanical process of the rock structure is evaluated by the quasi-static equilibrium equation and the typical Hooke's law, given by

$$-\nabla \cdot \boldsymbol{\sigma} = \boldsymbol{F}_v, \tag{6}$$

$$\boldsymbol{\sigma} = \boldsymbol{E} : \boldsymbol{\varepsilon} \ , \tag{7}$$

where $\boldsymbol{\sigma}$ [Pa] is the stress tensor, $\boldsymbol{F}_v$ [Pa m^{-1}] is the body force, $\boldsymbol{E}$ [Pa] is the elasticity tensor, and $\boldsymbol{\varepsilon}$ [-] is the strain tensor. In this work, the thermal stress and the inelastic behavior are disregarded for simplicity. A self-weight analysis is conducted to obtain the initial stress field, while the change in stress distribution by the cavity excavation is calculated using these equations. .

The advection-diffusion equation is used to calculate the solute transport behavior. The mechanical dispersion and the retardation due to the sorption processes are not considered here.

$$\frac{\partial (c_i \phi)}{\partial t} + \boldsymbol{u} \cdot \nabla c_i = \nabla \cdot (\phi \tau \boldsymbol{D}_{b,i} \nabla c_i) + R_i, \tag{8}$$

where c_i [mol m^{-3}] is the concentration of solute i, τ [-] is the coefficient related to tortuosity, $\boldsymbol{D_{b,i}}$ [m^2 s^{-1}] is the diffusion coefficient tensor, and R_i [mol m^{-3} s^{-1}] is the solute source or sink of solute i. The diffusion coefficient is controlled by the system temperature and can be defined by an Arrhenius-type equation [26], as

$$D_{b,i} = D_{b,i}^{0} \exp(-E_{D,i} / RT), \quad (9)$$

where $D_{b,i}^{0}$ [m^2 s^{-1}] and $E_{D,i}$ [J mol^{-1}] are the pre-exponential factor and the activation energy of the diffusion of solute *i*, respectively, and R [J mol^{-1} K^{-1}] is the gas constant.

The source/sink term, R_i, is calculated by considering both free-face dissolution/precipitation and pressure dissolution, and can be expressed by

$$R_i = R_i^{FF} + R_{diss,i}^{PS}, \quad (10)$$

where R_i^{FF} and $R_{diss,i}^{PS}$ [mol m^{-3} s^{-1}] are the rates of free-face dissolution/precipitation and pressure dissolution, respectively. They are the physical quantities that describe the mineral dissolution and precipitation per volume and time. The rate of the free-face dissolution/precipitation is defined by [10]

$$R_i^{FF} = k_+ A (a_{H^+})^n (1 - Q/K), \quad (11)$$

where k_+ [mol m^{-2} s^{-1}] is the mineral dissolution rate constant, A [m^2 m^{-3}] is the specific surface area, a_{H+} [-] is the activity of H^+, and n [-] is the constant, which may be obtained from experimental observations in the literature. Q [-] is the ionic activity product and K [-] is the equilibrium constant. When Q/K <1, free-face dissolution occurs; when Q/K >1, free-face precipitation occurs. The specific surface area is obtained by the measurement using the BET method, given as follows:

$$A = A_{BET}\,\rho_m, \tag{12}$$

where A_{BET} [m^2 kg^{-1}] is the specific surface area determined by the BET method.

In this work, the rock is assumed to be composed purely of quartz, and subscript *i* in Eqs. (8) - (10) is omitted hereinafter. The equilibrium and the dissolution rate constants in Eq. (11) are obtained from PHREEQC [27] and Rimstidt and Barnes (1980) [28], respectively. These constants are temperature-dependent and are given via polynomial approximation and by an Arrhenious expression, as follows:

$$K = \sum_{m=0}^{7} \alpha_m T^m, \tag{13}$$

$$k_+ = k_+^0 \exp(-E_{k_+}/RT), \tag{14}$$

where α_m (m=0-7) [-] is the constant, k^0_+ [mol m^{-2} s^{-1}] is the pre-exponential factor, and E_{k+} [J mol^{-1}] is the activation energy of the mineral dissolution.

Incorporating the process of pressure dissolution into the developed model is the most important task in this work. As described above, we have developed conceptual models that describe the process [20]-[24]. The flux that represents the pressure dissolution is driven by the gradient in the chemical potential between the highly-stressed contacts and the less-stressed site of the pore walls [13], [26]. Dissolution is most conveniently defined in terms of a dissolution mass flux, $\dot{M}_{diss}^{PS}$, the rate of addition of dissolved mass into solution at the interface, given as [20]

$$\dot{M}_{diss}^{PS} = \frac{3V_m^2(\sigma_a - \sigma_c)k_+\rho_g A_c}{RT}, \tag{15}$$

where V_m is the molar volume of the solid (2.27×10^{-5} m^3 mol^{-1} for quartz), σ_a [Pa] is the disjoining pressure [29] equal to the amount by which the pressure acting at the contacts exceeds the hydrostatic pore pressure, ρ_g is the grain density (2650 kg m^{-3} for quartz), A_c [m^2] is the area of the grain contact, and σ_c [Pa] is the critical stress, which defines the stress state where the compaction of the grain aggregate will effectively halt [20]. This stress is determined by considering the energy balance under applied stress and temperature conditions, given by [26], [30]

$$\sigma_c = \frac{E_m\left(1 - T/T_m\right)}{4V_m}, \tag{16}$$

where E_m and T_m are the heat and temperature of fusion, respectively (E_m = 8.57 kJ mol^{-1}, T_m = 1883 K for quartz).

Based on Eq. (15), the rate of the pressure dissolution, R_{diss}^{PS}, is derived through the following procedure. Firstly, the strain rate due to the pressure dissolution is given as [20]

$$\dot{\varepsilon}_{diss}^{PS} = \frac{\dot{M}_{diss}^{PS}}{d\,\rho_g A_c} = \frac{3V_m^2 k_+}{RTd}\left(\frac{\sigma_{eff}}{R_c} - \sigma_c\right), \tag{17}$$

$$\sigma_a = \frac{\sigma_{eff}}{R_c}, \tag{18}$$

where $\dot{\varepsilon}_{diss}^{PS}$ [-] is the strain state, d [m] is the grain diameter, σ_{eff} [Pa] is the effective stress exerted in the representative element, and R_c ($0 < R_c < 1$) [-] is the contact-area ratio. In this work,

203 the FE analyses are conducted with 2-D meshes in the following sections. To this end, the
204 effective stress is replaced with the von Mises stress that can boil any complex stress conditions
205 down to a single representative scalar value. Therefore, Eq. (17) may be expressed as

206 $$\dot{\varepsilon}_{diss}^{PS} \approx \frac{3V_m^2 k_+}{RTd}\left(\frac{\sigma_{VM}}{R_c} - \sigma_c\right), \tag{19}$$

207 $$\sigma_{VM} = \sqrt{\frac{3}{2}\boldsymbol{\sigma}:\boldsymbol{\sigma}}\,, \tag{20}$$

208 where σ_{VM} [Pa] is the von Mises stress. When the system is assumed to be simple cubic packing
209 with uniformly sized contacting spheres (**Figure 3**), the volumetric rate induced by the pressure
210 dissolution can be defined by

211 $$\dot{V}_{diss}^{PS} = \frac{\Delta d \cdot d^2}{\Delta t} = \dot{\varepsilon}_{diss}^{PS} d^3 = \frac{3V_m^2 k_+ d^2}{RT}\left(\frac{\sigma_{VM}}{R_c} - \sigma_c\right), \tag{21}$$

212 where $\dot{V}_{diss}^{PS}$ [m^3 s^{-1}] is the volumetric rate of the pressure dissolution. The dissolution rate, with
213 respect to the representative element, can be simply evaluated by dividing the volumetric rate by
214 the molar volume, as

215 $$\frac{\dot{V}_{diss}^{PS}}{V_m} = \frac{3V_m k_+ d^2}{RT}\left(\frac{\sigma_{VM}}{R_c} - \sigma_c\right). \tag{22}$$

216 The volume of the representative element (**Figure 3**) is d^3 [m^3], and the number of grains per unit
217 volume should be d^{-3} [m^{-3}]. Finally, the rate of pressure dissolution is defined by multiplying Eq.
218 (22) by d^{-3}, as follows:

$$R_{diss}^{PS} = \frac{3V_m k_+}{RTd}\left(\frac{\sigma_{VM}}{R_c} - \sigma_c\right). \quad (23)$$

As the pressure dissolution proceeds, contact-area ratio R_c increases and corresponding porosity ϕ decreases. Therefore, the relation between R_c and ϕ should be obtained to solve Eq. (23) with time. By considering the geometrical scheme (see **Figure 3** and more details in Appendix A), it is given by

$$R_c = \frac{12}{\pi}(1-\phi) - 2. \quad (24)$$

Consequently, the rate of pressure dissolution is rearranged by substituting Eq. (24) into Eq. (23), as follows:

$$R_{diss}^{PS} = \frac{3V_m k_+}{RTd}\left(\frac{\sigma_{VM}}{(12/\pi)(1-\phi) - 2} - \sigma_c\right). \quad (25)$$

2.2 Modification of porosity and related permeability

In this work, the change in porosity is only induced by the free-face dissolution/precipitation and the pressure dissolution. The porosity rates evaluated by the two geochemical processes are defined by

$$\dot{\phi}^{FF} = V_m R^{FF}, \quad (26)$$

$$\dot{\phi}_{diss}^{PS} = -V_m R_{diss}^{PS}, \quad (27)$$

where $\dot{\phi}^{FF}$ and $\dot{\phi}_{diss}^{PS}$ [s^{-1}] are the porosity rates of the free-face dissolution/precipitation and the

pressure dissolution, respectively. Therefore, the porosity at an arbitrary time is evaluated using Eqs. (26) and (27), given by

$$\phi = \phi_i + \int \dot{\phi}^{FF} dt + \int \dot{\phi}^{PS}_{diss} dt \,, \tag{28}$$

where ϕ_i [-] is the initial porosity. Once the porosity is calculated, the related permeability is also evaluated by the Kozeny-Carman equation [31], as

$$k = k_i \frac{(1-\phi_i)^2}{(1-\phi)^2} \left(\frac{\phi}{\phi_i} \right)^3 , \tag{29}$$

where k and k_i [m^2] are the permeability at an arbitrary time and the initial permeability, respectively.

3. Model verification

In the previous section, we proposed a coupled THMC model to describe the evolution of porosity/permeability in porous media. In order to verify the proposed model, the model predictions are compared with the laboratory experiments performed by Elias and Hajash (1992) [19]. The compaction of quartz sand, with a mean grain diameter of 180-250 μm, has been completed under the constant effective stresses of 69.0, 34.5, and 17.2 MPa at 150°C. The changes in porosity and the silica concentrations in the pore fluid were measured over time to

253 examine the chemical and physical processes associated with the pressure solution [19]. In this
254 work, both the rates of porosity reduction and the evolving concentrations of silica in the pore
255 fluid were predicted. The parameters utilized in the calculations are summarized in **Table 1**.

256 In the predictions, the domain whose porosity initially starts with 0.35, equivalent to that of
257 the experiments [19], was set to be a square with side lengths of 0.01 m. The uniaxial confining
258 pressures of 69.0, 34.5, and 17.2 MPa and the temperature of 150°C were applied as the boundary
259 conditions and as the initial condition, respectively. The silica concentration within the domain
260 was initially fixed at the equilibrium concentration of quartz at 150°C, which was obtained by Eq.
261 (13), and was followed over time by considering the free-face dissolution/precipitation and/or the
262 pressure dissolution of quartz. All the boundaries were assumed to be thermally and hydraulically
263 the outflow boundaries. The initial contact-area ratio, R_{c0}, was evaluated by assuming the Herzian
264 contacts, given by

265 $$R_{c0} = \left(\frac{3\sigma_{eff}\,\pi\left(1-\nu\right)^2}{4E} \right)^{2/3}, \tag{30}$$

266 where σ_{eff} [Pa] is the effective stress (i.e., 69.0, 34.5, or 17.2 MPa), ν [-] is Poisson's ratio, and E
267 [Pa] is Young's modulus. When the pressure dissolution proceeds, the contact-area ratio increases.
268 The change is obtained using Eqs. (24), (26), and (27), as

$$
\begin{aligned}
R_c &= R_{c0} + \int \dot{R}_c dt \\
&= R_{c0} - \frac{12}{\pi} \int \dot{\phi} dt \\
&= R_{c0} - \frac{12}{\pi} \int \left(\dot{\phi}^{FF} + \dot{\phi}^{PS}_{diss} \right) dt \\
&= R_{c0} - \frac{12}{\pi} \left(\int V_m \cdot R^{FF} dt - \int V_m \cdot R^{PS}_{diss} dt \right)
\end{aligned}
\quad . \tag{31}
$$

After every time step, the new R_c was updated and used for calculating the rate of the pressure dissolution, R^{PS}_{diss}, in the following time step (see **Figure 2**). Note that in these verification predictions, R^{PS}_{diss} was evaluated over time with Eq. (23) instead of Eq. (25) because R_c can be evaluated directly with Eq. (31). It should also be noted that the specific surface area in Eq. (11) cannot be obtained from the literature [19]. Therefore, by introducing roughness factor f_r [32], which is the ratio of the true (microscopic) surface area over the apparent (geometric) surface area, the model predictions were conducted. The relation between specific surface area A and roughness factor f_r is defined as follows:

$$
A = f_r A_{geo}, \tag{32}
$$

where A_{geo} [m^2 m^{-3}] is the apparent specific surface area, which is simply given by the ratio of the surface area of the spherical grain of diameter d over the volume, as

$$
A_{geo} = \frac{\pi d^2}{\frac{\pi d^3}{6}} = \frac{6}{d}. \tag{33}
$$

In the model predictions, three kinds of roughness factors, namely, 10, 20, and 80, were utilized. The values are congruent with the magnitude indicated by Anbeek [1992] [33], who concluded

284 that it ranged from 2.5 to 11 for freshly created surfaces, and Sverdrup [1990] [34], who reported
285 that it varied between 1.5 and 71 for 28 silicate minerals.

286 Predictions of the porosity reduction rates and the silica concentration rates normalized by
287 the initial values are shown in **Figure 4** and **Figure 5**, respectively, together with the data
288 measured in the experiments. Surprisingly, all the predicted porosity reduction rates with time
289 closely match the experimental measurements (**Figure 4**). Note that changing the roughness factor
290 has little effect on the evolution of the porosity; and thus, the predictions with different roughness
291 factors are not shown in **Figure 4**. In contrast, the predicted silica concentrations are clearly
292 dependent on which roughness factors are applied (**Figure 5**). The utilization of higher roughness
293 factors results in the prediction of lower silica concentrations. The system in the pore fluid is
294 always oversaturated with silica because that is initially equivalent to the equilibrium
295 concentration, and the additional solute is supplied from the grain contacts via the pressure
296 dissolution. Therefore, the rates of precipitation are augmented by the higher roughness factors,
297 resulting in the lower silica concentrations. The predictions show some variations because of the
298 different roughness factors, but they follow the tendency observed in the experiments well (i.e.,
299 the abrupt increase after applying the pressures and the gradual decrease with time). Overall, a
300 comparison of the results of the porosity reduction and the evolving silica concentrations between
301 the predictions and the experimental measurements gives us confidence to use the developed

model to examine the long-term evolution of the porosity/permeability in porous media due to the free-face dissolution/precipitation and the pressure dissolution, dependent on the applied pressure, temperature, and flow conditions.

4. Long-term predictions of permeability

The developed model was applied to predict the long-term evolution of the permeability in sedimentary rock near radioactive wastes within a simulated repository. It should be noted that although we used actual data from related literature in the following predictions, we do not anticipate any specific sites for high-level radioactive waste repositories.

4.1 Modelling conditions

The calculation domain, of the rock density of 1700 kg/m^3, was set to be a rectangle with vertical and horizontal lengths of 700 and 12.2 m, respectively. The canisters of radioactive wastes were virtually installed as a heat source by setting them laterally at a depth of 450 m [35]. The horizontal length of 12.2 m was chosen for the domain because it may be one-half of the center-to-center spacing of each cavity, of the diameter 2.22 m [35] (**Figure 6**). The rock for the calculations was assumed to have been fully-saturated with water and to have been composed

purely of quartz, with the initial porosity of 0.40 [36]. The hydraulic and thermal gradients were set to be 1/1000 and 5°C/100 m, respectively [37]. The surface temperature was fixed at 15°C. The initial silica concentrations within the domain were assumed to be the equilibrium values, which were evaluated by Eq. (13). The change in pH was not considered and the initial value was set at pH = 7.

In this work, the Excavation Distributed Zone (EDZ) was modeled explicitly with respect to the rock permeability. The scientific and technical report, summarizing the HLW disposal construction in Japan [38], indicates that the EDZ in both sedimentary and crystalline rocks may range, in the radial direction, from the periphery of the excavated cavity to roughly 1 m. Therefore, the range of 0.8 m was modeled as the EDZ in our calculations (**Figure 6**). The permeability in the EDZ was increased by two orders of magnitude greater than the sound rock [35], [39]. Note that the thermal and the mechanical properties in the EDZ were assumed to be equivalent to those of sound rock, because those in the EDZ were ill-defined, and examining the changes in permeability due to geochemical processes is the most significant task in this work. In the actual calculations, the changes in the von Mises stresses, due to the excavation, were predicted by conducting a self-weight analysis (**Figure 7**). The evolved von Mises stresses, greater around the periphery of the cavity, as is apparent in **Figure 7**, are the driving-force for the pressure dissolution (see Eq. (25)). The heat source from the radioactive wastes was modeled by applying

338 the temperatures at the periphery of the cavity as the boundary conditions. The applied
339 temperatures over time were obtained from the literature [38], as shown in **Figure 8**. The
340 prediction period was set at 10^4 years after the excavation. All the boundaries, excluding the
341 periphery of the cavity, were assumed to be thermally and hydraulically the outflow boundaries.
342 The parameters utilized in the calculations are summarized in **Table 2**.
343
344 *4.2 Prediction results*
345 In this work, the predictions were conducted for two different cases – one was done by
346 considering the full processes illustrated in **Figure 2**, and the other was done by excluding only
347 the pressure dissolution, in order to examine the effect of the pressure dissolution on the change in
348 permeability with time. The former and the latter cases are called the “PS” and the “no-PS”
349 conditions hereinafter. Calculations for the no-PS condition were performed by merely making
350 R_{diss}^{PS} in Eq. (25) zero at all the calculation steps.
351 The change in the temperature distribution with time, predicted under the PS condition, is
352 shown in **Figure 9**. The temperature in the EDZ increases with time; it increases to more than
353 80°C between 10^1 and 10^2 years. Subsequently, it decreases with time and reaches a steady
354 temperature (i.e., ~45°C) after 10^4 years. This tendency is quite similar to the change in Si
355 concentration with time (**Figure 10**), which is reasonable. As the equilibrium concentration of Si

356 is only controlled by the induced temperature, the changes over time should be similar. It should
357 be noted that the predicted changes in both temperature and the Si concentration with time, under
358 the no-PS condition, show no great difference from those under the PS condition. This is because
359 the concentrations in the whole system approach the equilibrium values in a relatively short
360 period, through free-face precipitation, when additional solute is supplied in the pore fluid due to
361 the pressure dissolution, and through free-face dissolution, when the system temperature and the
362 related equilibrium concentration increase. Consequently, the Si concentrations are equivalent to
363 the equilibrium values throughout most of the calculation period.

364 The changes in permeability with time under the no-PS and the PS conditions are compared
365 (**Figure 11** and **Figure 12**). Note that the permeability is normalized by the initial value. As is
366 apparent from the figures, it changes little with time under the no-PS condition, while it decreases
367 with time and the reduction appears after 10^2 years under the PS condition. Specifically, the
368 reduction is significant within the EDZ. This is because the pressure dissolution, resulting in
369 porosity reduction, is enhanced by the increase in the von Mises stress due to the cavity
370 excavation (see **Figure 7**), and an additional reduction in porosity is caused by the free-face
371 precipitation induced by the supply of the dissolved silica through the pressure dissolution. In
372 order to further investigate the influence of the pressure dissolution on the permeability change
373 within the EDZ, the changes with time at four specific locations, shown in **Figure 13**, are depicted

374 in **Figure 14**. Three of the four points are located within the EDZ, and the fourth one is 5 m away
375 from the periphery of the cavity. No change in permeability is observed under the no-PS condition.
376 In reality, the free-face precipitation of the secondary minerals, induced by the dissolution of the
377 cement materials, may cause changes in the porosity/permeability, but it is not the case in this
378 work. On the other hand, the permeability at No. 1 decreases by one order of magnitude in 10^4
379 years. However, the reduction is locally limited and is not observed at No. 4, which is located at
380 one-fourth of the center-to-center spacing of each cavity (**Figure 14**). In the current predications,
381 the decrease in permeability was observed only under the PS condition. This should result in the
382 delay of the transportation of radioactive materials, and the influence needs to be examined
383 quantitatively.

384 As a parametric study, predictions are made by varying the parameters of initial porosity ϕ_i
385 and critical stress σ_c, that should control the rate of the pressure dissolution (see Eq. (25)) to
386 examine the influence on the change in permeability. Two different initial porosities, 0.40 and
387 0.45, are selected to simulate Horonobe mudstone in Japan [36], and three levels of critical stress,
388 15, 50, and 80 MPa, are set for the analysis. The change in permeability at observation point No. 1,
389 shown in **Figure 13**, is shown in **Figure 15**. It is obvious that when a higher critical stress is
390 applied, less change in permeability is observed. This is because the effect of the pressure
391 dissolution becomes smaller when the difference between the von Mises stress and the critical

392 stress is smaller, as is clear from Eq. (25). In particular, at 80 MPa, the permeability hardly
393 changes in the case of ϕ_i = 0.40, and it decreases roughly 30 % for 10^4 years in the case of 0.45.
394 From the above calculations, we have confirmed that choosing the right values for the critical
395 stress is of great importance to achieving precise predictions.
396
397
398 **5. Conclusions**
399 A coupled THMC model was developed to investigate the long-term evolution of the
400 permeability in sedimentary rocks. The model solves the heat transfer, the groundwater flow, the
401 variation in induced stresses, and the geochemical reactions (i.e., the free-face
402 dissolution/precipitation and the pressure dissolution), and their interactions. The changes in
403 porosity and silica concentration in the quartz aggregates were examined to test the adequacy of
404 the developed model in representing the experimentally observed behavior [19]. The predictions
405 showed an excellent agreement with the experimental observations. Subsequently, the verified
406 model was applied to examine the influence of the pressure dissolution on the evolution of the
407 permeability in sedimentary rocks where a radioactive waste repository may be constructed, in
408 considering the expected temperature, flow, and stress conditions. The predictions confirmed that
409 the process of the pressure dissolution decreased the permeability especially close to the

410 excavated cavity by one order of magnitude smaller than the initial value, which should delay the
411 transportation of the radioactive materials.

412 The developed model is straightforward and relatively simple because some interactions
413 among the THMC processes are omitted, but it enables the long-term evolution of the
414 permeability under arbitrary stress and temperature conditions to be followed over time with some
415 precision. Generally, when considering coupling processes for solving complicated nonlinear
416 problems, the uncertainty should be significant. Therefore, it is always important to ponder
417 whether complex, fully-coupled models are necessary for achieving sufficiently high precision. In
418 the near future, we will update the current model by taking into account the omitted processes
419 among the THMC interactions (e.g., the hydraulic-mechanical interactions; see **Figure 1**), and
420 examine whether or not the updates are indeed meaningful to the problems of interest.

421

422

423 **Acknowledgments**

424 This work was supported by JSPS KAKENHI, Grant Nos. 26249139 and 25630413, and by
425 the Basic Research and Development Project of the Korea Institute of Geoscience and Mineral
426 Resources (KIGAM, Project Code No. GP2015-010), which was funded by the Ministry of
427 Science, ICT & Future Planning, Korea. Their support is gratefully acknowledged. The data used

428 in this work are available upon request from the authors.

429

430

431 **APPENDIX A: Relation between contact-area ratio and porosity**

432 Solid volume V_s, in the representative elementary volume, is obtained by subtracting the
433 sums of the volumes truncated between the contacts of two hemispheres from the volume of a
434 sphere of diameter d, given by

435 $$V_s = \frac{1}{6}\pi h(3a^2 + \frac{3d^2}{4} + h^2), \tag{A1}$$

436 where h is one-half of the domain height and a is the radius of the contact area. One-half of the
437 domain height, h, is given by

438 $$h = \sqrt{\frac{d^2}{4} - a^2}\,. \tag{A2}$$

439 The porosity, ϕ, is obtained by subtracting the solid volume, V_s, divided by the total volume of the
440 domain, V_t, from one, as follows:

441 $$\phi = 1 - \frac{V_s}{V_t} = 1 - \frac{\frac{1}{6}\pi\sqrt{\frac{d^2}{4} - a^2}(2a^2 + d^2)}{d^2\sqrt{\frac{d^2}{4} - a^2}} = 1 - \frac{\pi(2a^2 + d^2)}{6d^2}\,. \tag{A3}$$

442 The radius of the contact area is expressed by

443 $$a^2 = \frac{d^2}{4}R_c\,. \tag{A4}$$

444 By substituting Eq. (A3) into Eq. (A2), porosity ϕ is rearranged as

$$\phi = 1 - \frac{\pi\left(\frac{d^2}{2}R_c + d^2\right)}{6d^2} = 1 - \left\{\frac{\pi}{12}(R_c + 2)\right\}. \quad \text{(A5)}$$

$$\Rightarrow R_c = \frac{12}{\pi}(1-\phi) - 2\,. \quad \text{(A6)}$$

Nomenclature

A	specific surface area [$m^2\ m^{-3}$]
A_{BET}	specific surface area determined by the BET method [$m^2\ kg^{-1}$]
A_c	area of the grain contact [m^2]
A_{geo}	apparent specific surface area [$m^2\ m^{-3}$]
a_{H+}	activity of H^+ [-]
C_i	concentration of the solute i [mol m^{-3}]
$C_{p,m}$	heat capacity of the solid [J $kg^{-1}\ K^{-1}$]
$C_{p,w}$	heat capacity of the fluid [J $kg^{-1}\ K^{-1}$]
D	potential head of the fluid [m]
$\boldsymbol{D_{b,i}}$	diffusion coefficient tensor [$m^2\ s^{-1}$]
d	grain diameter [m]
$\boldsymbol{E}$	elasticity tensor [Pa]
$E_{D,i}$	activation energy of the diffusion of the solute i [J mol^{-1}]
E_{k+}	activation energy of the mineral dissolution [J mol^{-1}]
E_m	heat of fusion [kJ mol^{-1}]
$\boldsymbol{F_v}$	body force [Pa m^{-1}]
f_m	source term for flow [kg $m^{-3}\ s^{-1}$]
f_r	roughness factor [-]
g	gravity acceleration [m s^{-2}]
K	equilibrium constant [-]
$\boldsymbol{k}$	rock permeability tensor [m^2]
$\boldsymbol{k_{eq}}$	equilibrium thermal conductivity tensor [W $m^{-1}\ K^{-1}$]

$\boldsymbol{k_m}$	thermal conductivity tensor of the solid [W m^{-1} K^{-1}]
$\boldsymbol{k_w}$	thermal conductivity tensor of the fluid [W m^{-1} K^{-1}]
k_+	dissolution rate constant [mol m^{-2} s^{-1}]
$\dot{M}_{diss}^{PS}$	rate of addition of dissolved mass into solution at the interface [kg s^{-1}]
p	fluid pressure [Pa]
Q	ionic activity product [-]
Q_h	heat source [W m^{-3}]
R	gas constant [J mol^{-1} K^{-1}]
R_c	contact-area ratio [-]
R_i^{FF}	rate of free-face dissolution/precipitation of the solute *i* [mol m^{-3} s^{-1}]
$R_{diss,i}^{PS}$	rate of pressure dissolution of the solute *i* [mol m^{-3} s^{-1}]
R_i	solute source or sink of the solute *i* [mol m^{-3} s^{-1}]
T	system temperature [K]
T_m	temperature of fusion [K]
$\boldsymbol{u}$	fluid velocity tensor [m s^{-1}]
$\dot{V}_{diss}^{PS}$	volumetric rate of the pressure dissolution [m^3 s^{-1}]
V_m	molar volume [m^3 mol^{-1}]
V_s	solid volume [m^3]

Greek letters

$\boldsymbol{\varepsilon}$	strain tensor [-]
$\dot{\varepsilon}_{diss}^{PS}$	strain rate due to the pressure dissolution [s^{-1}]

494	ϕ	porosity [-]
495	$\dot{\phi}^{FF}$	porosity rate of the free-face dissolution/precipitation [s^{-1}]
496	$\dot{\phi}_{diss}^{PS}$	porosity rate of the pressure dissolution [s^{-1}]
497	μ	dynamic viscosity of the fluid [Pa s]
498	ν	Poisson's ratio [-]
499	ρ_g	grain density [kg m^{-3}]
500	ρ_m	density of the solid [kg m^{-3}]
501	ρ_w	density of the fluid [kg m^{-3}]
502	$(\rho C_p)_{eq}$	equilibrium volumetric heat capacity [J K^{-1} m^{-3}]
503	$\boldsymbol{\sigma}$	stress tensor [Pa]
504	σ_a	stress acting at the contact area [Pa]
505	σ_c	critical stress [Pa]
506	σ_{eff}	effective stress [Pa]
507	σ_{VM}	von Mises stress [Pa]
508	τ	tortuosity [-]

509

6. References

[1] Tsang CF (ed.). Coupled Processes Associated with Nuclear Waste Repositories. Elsevier 2012; ISBN 9780323142403: 816 pp.

[2] Tsang Y. Effects of coupled processes on a proposed high-level radioactive waste repository at Yucca Mountain, Nevada. Geological Society of America Memoirs 2012; 209:363-393.

[3] Zheng L, Samper J. A coupled THMC model of FEBEX mock-up test. Phys Chem Earth 2008; 33:S486–S498.

[4] Taron J, Elsworth D, Min K-B. Numerical simulation of thermal-hydrologic-mechanical-chemical processes in deformable, fractured porous media. Int J Rock Mech Min Sci 2009; 46:842-854.

[5] Nasir O, Fall M, Evgin E. A simulator for modeling of porosity and permeability changes in near field sedimentary host rocks for nuclear waste under climate change influences. Tunnelling Underground Space Technol 2014; 42:122-135.

[6] Kim J, Sonnenthal E, Rutqvist J. A sequential implicit algorithm of chemo-thermo-poro-mechanics for fractured geothermal reservoirs. Comput Geotech 2015; 76:59-71.

[7] Lang PS, Paluszny A, Zimmerman RW. Hydraulic sealing due to pressure solution contact zone growth in siliciclastic rock fractures. J Geophys Res 2015; 120:4080 -

528 4101,doi:10.1002/2015JB011968.

529 [8] McDermott C, Bond A, Harris, AF, Chittenden N, Thatcher K. Application of hybrid
530 numerical and analytical solutions for the simulation of coupled thermal, hydraulic,
531 mechanical and chemical processes during fluid flow through a fractured rock. Environ Earth
532 Sci 2015; DOI 10.1007/s12665-015-4422-7.

533 [9] Taron J, Elsworth D. Coupled mechanical and chemical processes in engineered geothermal
534 reservoirs with dynamic permeability. Int J Rock Mech Min Sci 2010; 47:1339-1348.

535 [10] Lasaga AC. Chemical Kinetics of Water-Rock Interactions. J Geophys Res 1984;89:
536 4009-4025.

537 [11] Croizé D, Renard F, Bjørlykke K, Dysthe DK. Experimental calcite dissolution under stress:
538 evolution of grain contact microstructure during pressure solution creep. J Geophys Res
539 2010; 115, B09207, doi:10.1029/2010JB000869.

540 [12] Neveux L, Grgic D, Carpentier C, Pironon J, Truche L, Girard JP. Experimental simulation
541 of chemomechanical processes during deep burial diagenesis of carbonate rocks. J Geophys
542 Res 2014; 119, 984.1007, doi:10.1002/2013JB010516.

543 [13] Raj R. Creep in polycrystalline aggregates by matter transport though a liquid phase. J
544 Geophys Res 1982; 87:4731-4739.

545 [14] Robin P-Y F. Pressure solution at grain to grain contacts. Geochim Cosmochim Acta 1978;

546 42:1383-1389.

547 [15] Spiers CJ, De Meer S, Niemeijer AR, Zhang X. Kinetics of Rock Deformation by Pressure
548 Solution and the Role of Thin Aqueous Films. In: Frontiers Science Series 2003:129e158.

549 [16] Weyl PK. Pressure solution and force of crystallization-A phenomenological theory. J
550 Geophys Res 1959; 64:2001-2025.

551 [17] Zhang X, Spiers CJ, Peach CJ. Compaction creep of wet granular calcite by pressure
552 solution at 28 C to 150 C. J Geophys Res 2010; 115 (B9):B09217.

553 [18] Zubtsov S, Renard F, Gratier JP, Guiguet R, Dysthe DK, Traskine V. Experimental pressure
554 solution compaction of synthetic halite/calcite aggregates. Tectonophysics 2004; 385:45-57.

555 [19] Elias BP, Hajash A. Change in quartz solubility and porosity change due to effective stress:
556 An experimental investigation of pressure solution. Geology 1982; 20:451-454.

557 [20] Yasuhara H, Elsworth D, Polak A. A mechanistic model for compaction of granular
558 aggregates moderated by pressure solution. J Geophys Res 2003; 108(11):2530,
559 doi:10.1029/2003JB002536.

560 [21] Yasuhara H, Elsworth D, Polak A. Evolution of permeability in a natural fracture: The
561 significant role of pressure solution. J Geophys Res 2004; 109(B3):B03204,
562 doi:10.1029/2003JB002663.

563 [22] Yasuhara H, Elsworth D, Polak A, Liu J, Grader A, Halleck P. Spontaneous Permeability

564 Switching in Fractures in Carbonate: Lumped Parameter Representation of Mechanically-
565 and Chemically-Mediated Dissolution. Transp Porous Media 2006; 65:385-409.
566 [23] Yasuhara H, Elsworth D. Compaction of a rock fracture moderated by competing roles of
567 stress corrosion and pressure solution. Pure Appl. Geophys 2008; 165:1289-1306.
568 [24] Yasuhara H, Kinoshita N, Ohfuji H, Lee DS, Nakashima S, Kishida K. Temporal alteration
569 of fracture permeability in granite under hydrothermal conditions and its interpretation by
570 coupled chemo-mechanical model. Appl Geochem 2011; 26:2074-2088.
571 [25] COMSOL2014 : COMSOL MULTIPHYSICS. Version 5.0, Available from
572 www.comsol.com.
573 [26] Revil A. Pervasive pressure-solution transfer: a poro-visco-plastic model. Geophys Res Lett
574 1999; 26:255-258.
575 [27] Parkhurst DL, Appelo CAJ. Description of Input and Examples for PHREEQC Version 3-A
576 Computer Program for Speciation, Batch-Reaction, One-Dimensional Transport, and Inverse
577 Geochemical Calculations, Online version available from
578 http://wwwbrr.cr.usgs.gov/projects/GWC_coupled/phreeqc/phreeqc3-html/phreeqc3.htm.
579 [28] Rimstidt JD, Barnes HL. The kinetics of silica-water reactions. Geochim Cosmochim Acta
580 1980; 44:1683-1699.
581 [29] Heidug WK. Intergranular solid-fluid phase transformations under stress: The effect of

582 surface forces. J Geophys Res 1995; 100:5931-5940.
583 [30] Stephenson LP, Plumley WJ, Palciauskas VV. A model for sandstone compaction by grain
584 interpenetration. J Sediment Petrol 1992; 62:11-22.
585 [31] Bear J. Dynamics of Fluids in Porous Media. Dover Publications Inc. 1972:166.
586 [32] Murphy WM, Helgeson HC. Thermodynamic and kinetic constraints on reaction rates
587 among minerals and aqueous solutions. IV. Retrieval of rate constants and activation
588 parameters for the hydrolysis of pyroxene, wollastonite, olivine, andalusite, quartz, and
589 nepheline. Am J Sci 1989; 289:17-101.
590 [33] Anbeek C. Surface roughness of minerals and implications for dissolution studies. Geochim
591 Cosmochim Acta 1992; 56:1461-1469.
592 [34] Sverdrup H. The Kinetics of Base Cation Release Due to Chemical Weathering. Lund
593 University Press, Lund, Sweden 1990:245pp.
594 [35] Suzuki H, Nakama S, Fujita T, Imai H, Sazarshi M. A long-term THMC assessment on the
595 geochemical behavior of the bentonite buffer. J Nucl Fuel Cycle Environ 2012; 19:39-50.
596 [36] Miyazawa D, Sanada H, Kiyama T, Sugita Y, Ishijima Y. Poroelastic coefficients for
597 siliceous rocks distributed in the Horonobe area, Hokkaido, Japan. J MMIJ 2011;
598 127:132-138.
599 [37] Kamei G, Honda A, Mihara M, Oda C, Murakami H, Masuda K, Yamaguchi K, Matsuda S,

600 Ichige S, Takahashi K, Meguro Y, Yamaguchi H, Sakakibara T, Sasaki T. Research and
601 development for treatment and disposal technologies of TRU waste JFY 2007 annual report.
602 JAEA-research 2008-082:1-84.
603 [38] Japan Nuclear Cycle Development Institute, 2000. Second Progress Report on Research and
604 Development for the Geological Disposal of HLW in Japan, Supporting Report 2 Repository
605 Design and Engineering Technology, H12: Project to Establish the Scientific and Technical
606 Basis for HLW Disposal in Japan. JNC TN1410 2000-003, IV-139-IV-160.
607 [39] Minato K (ed.). JAEA R&D review 2013; ISSN 2188-1456.
608
609

List of Tables

615

616 Table 1. Calculation parameters to simulate experimental results.

Diameter d [μm]	Temperature T [°C]	Effective stress σ_{eff} [MPa]	Critical stress σ_c [MPa]	Equilibrium constant K [mol m^{-3}]
215	150	69.0, 34.5, 17.2	73.2	1.79

Diffusion coefficient D_b [m^{2}s^{-1}]	Dissolution rate constant k_+ [mol m^{-2} s^{-1}]	Young's modulus E [GPa]	Poisson's ratio ν [-]
1.12×10^{-9}	2.51×10^{-9}	72.4	0.17

617

618

619 Table 2. Calculation parameters to simulate long-term permeability.

Rock type	Initial permeability k_i [m^2]	Young's modulus E [GPa]	Poisson's ratio ν [-]	Initial porosity ϕ_i [-]	Thermal conductivity k_{eq} [W m^{-1} K^{-1}]	Heat capacity C_p [J kg^{-1} K^{-1}]
EDZ	1.0×10^{-13}	2.5	0.30	0.40	1.60	1500
Sound	1.0×10^{-15}	2.5	0.30	0.40	1.60	1500

620

621

List of Figures

640 periphery of the cavity [38].

641 Figure 9. Change in temperature distribution with time in the range of 100 to 104 years under the
642 PS condition.

643 Figure 10. Change in Si concentration distribution with time in the range of 100 to 104 years
644 under the PS condition.

645 Figure 11. Change in normalized permeability with time in the range of 100 to 104 years under
646 the no-PS condition. No permeability change is confirmed.

647 Figure 12. Change in normalized permeability with time in the range of 100 to 104 years under
648 the PS condition. The permeability decreases with time. The reduction is especially significant
649 around the periphery of the cavity.

650 Figure 13. Specific locations where changes in permeability with time are observed.

651 Figure 14. The permeability changes with time at specific locations indicated in Figure 13((a) the
652 no PS condition and (b) the PS condition).

653 Figure 15. The permeability changes with time under the PS condition at No. 1, indicated in
654 Figure 13((a) initial porosity of 0.40 and (b) 0.45).

655

656

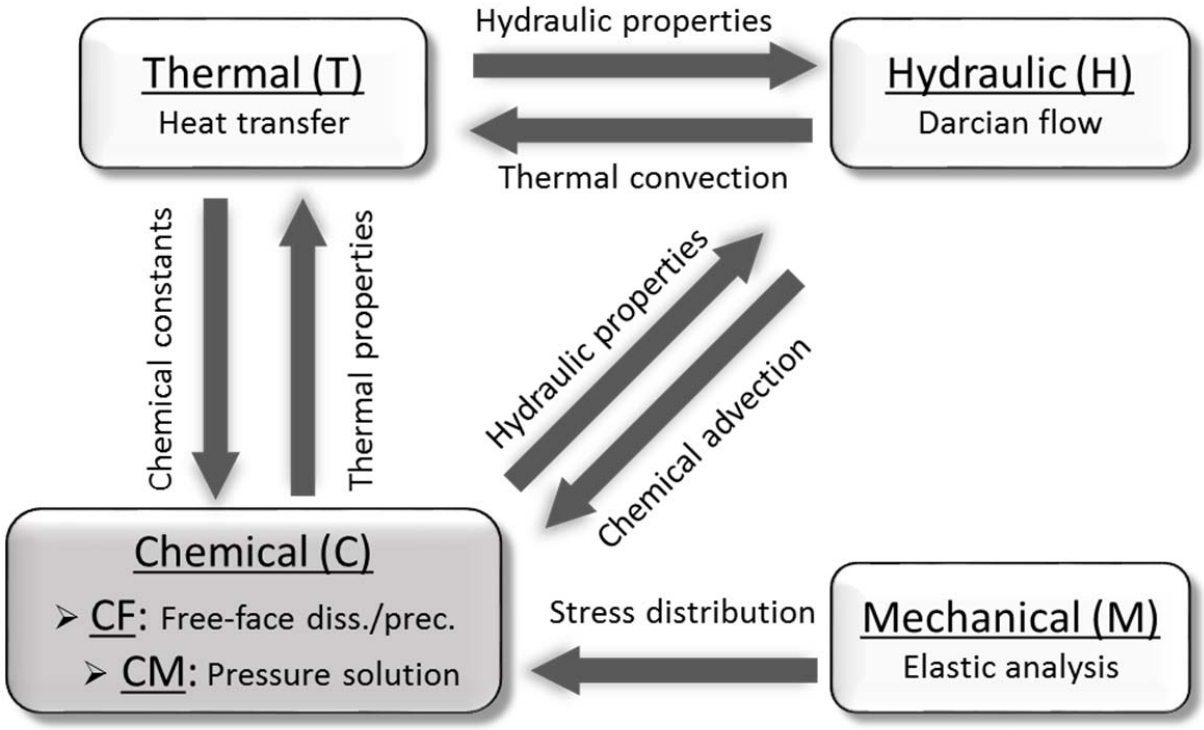

657

658 Figure 1. THMC interactions considered in the developed numerical model.

659

660

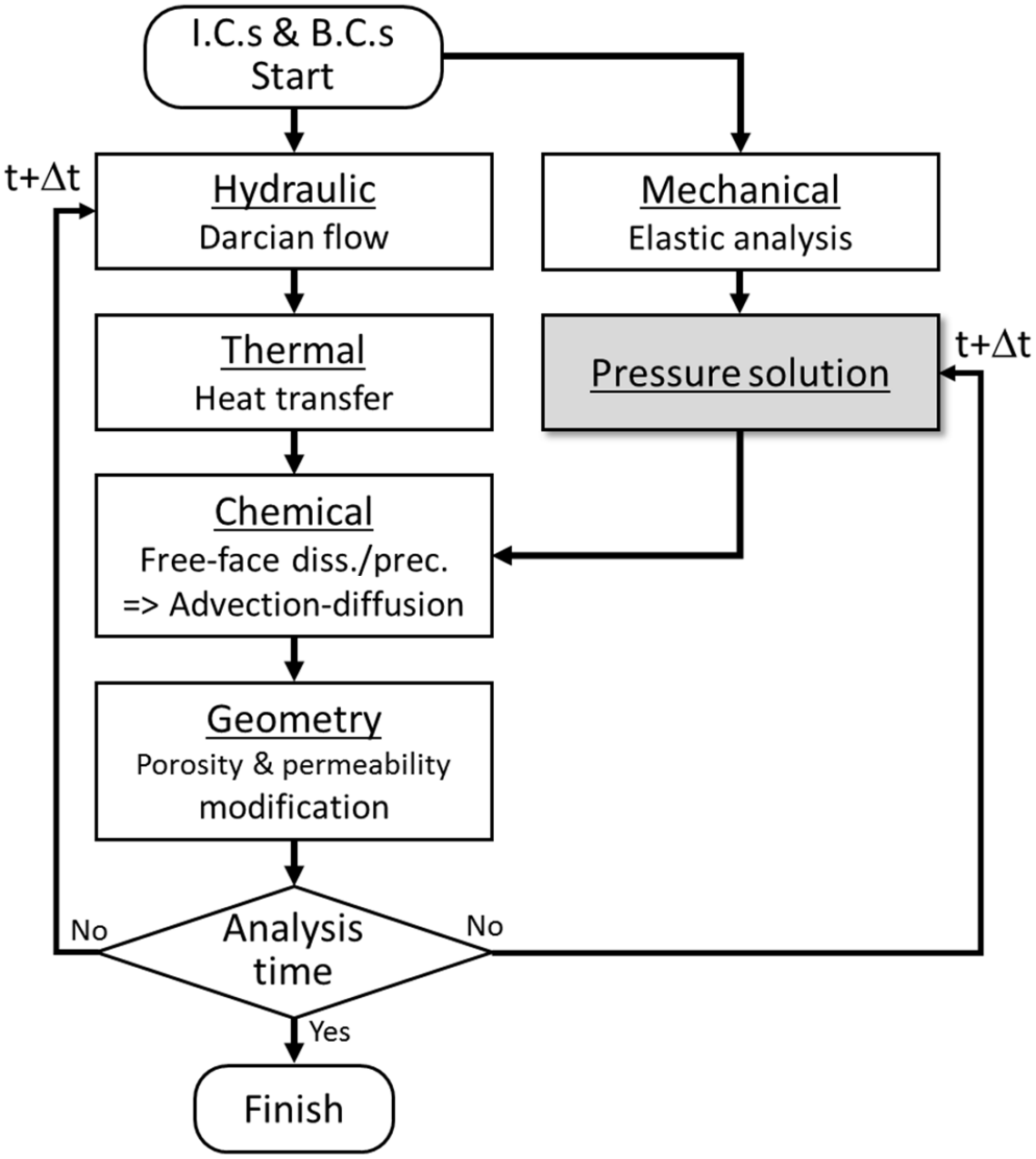

661

662 Figure 2. Sequential procedure to conduct consistent calculations of porosity change with time.

663

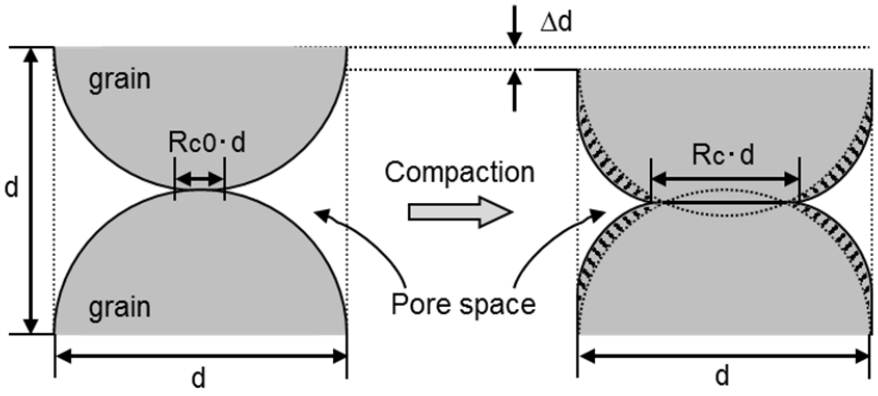

Figure 3. Geometrical model of grain-to-grain contact. Initially, two grains contact each other with an initial contact-area ratio of R_{c0}. As compaction proceeds due to the pressure solution, contact-area ratio R_c increases and free-face dissolution/precipitation occurs simultaneously, resulting in porosity modification.

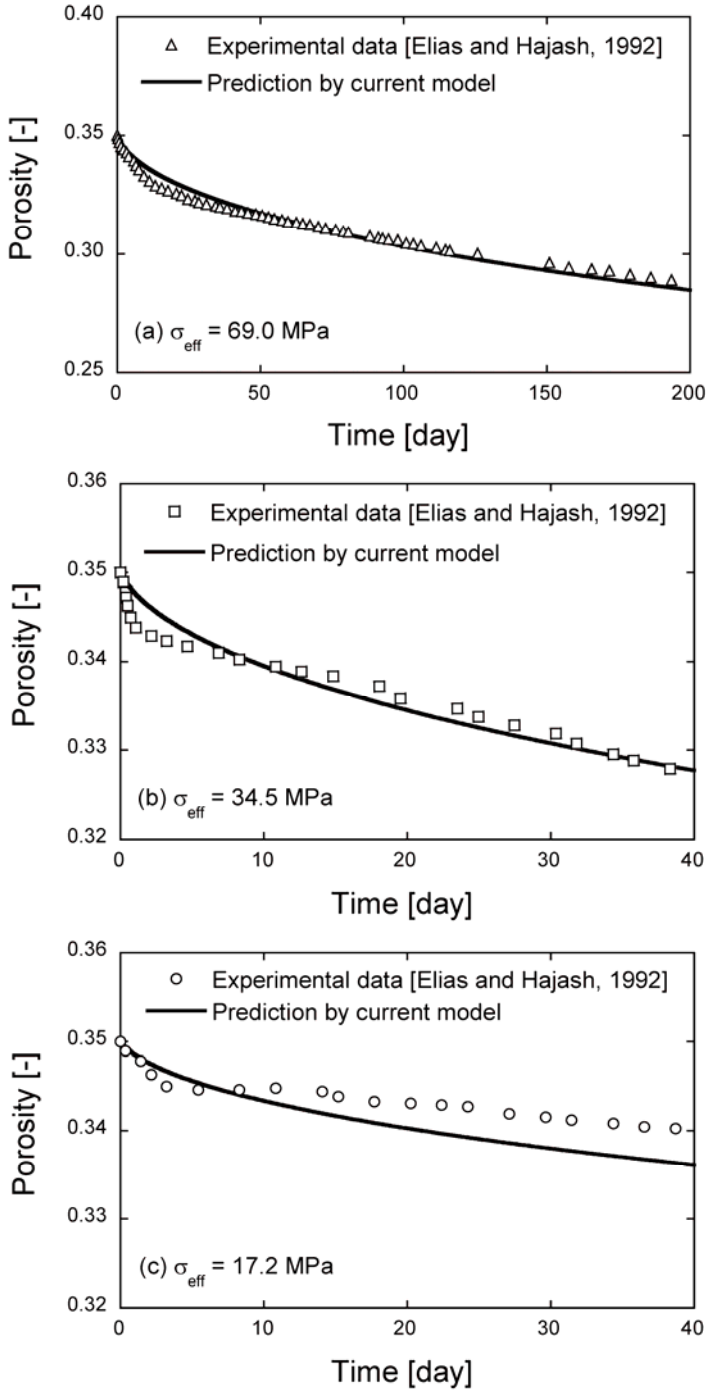

Figure 4. Comparison of porosity reduction with time between experimental data [19] and predictions of the model.

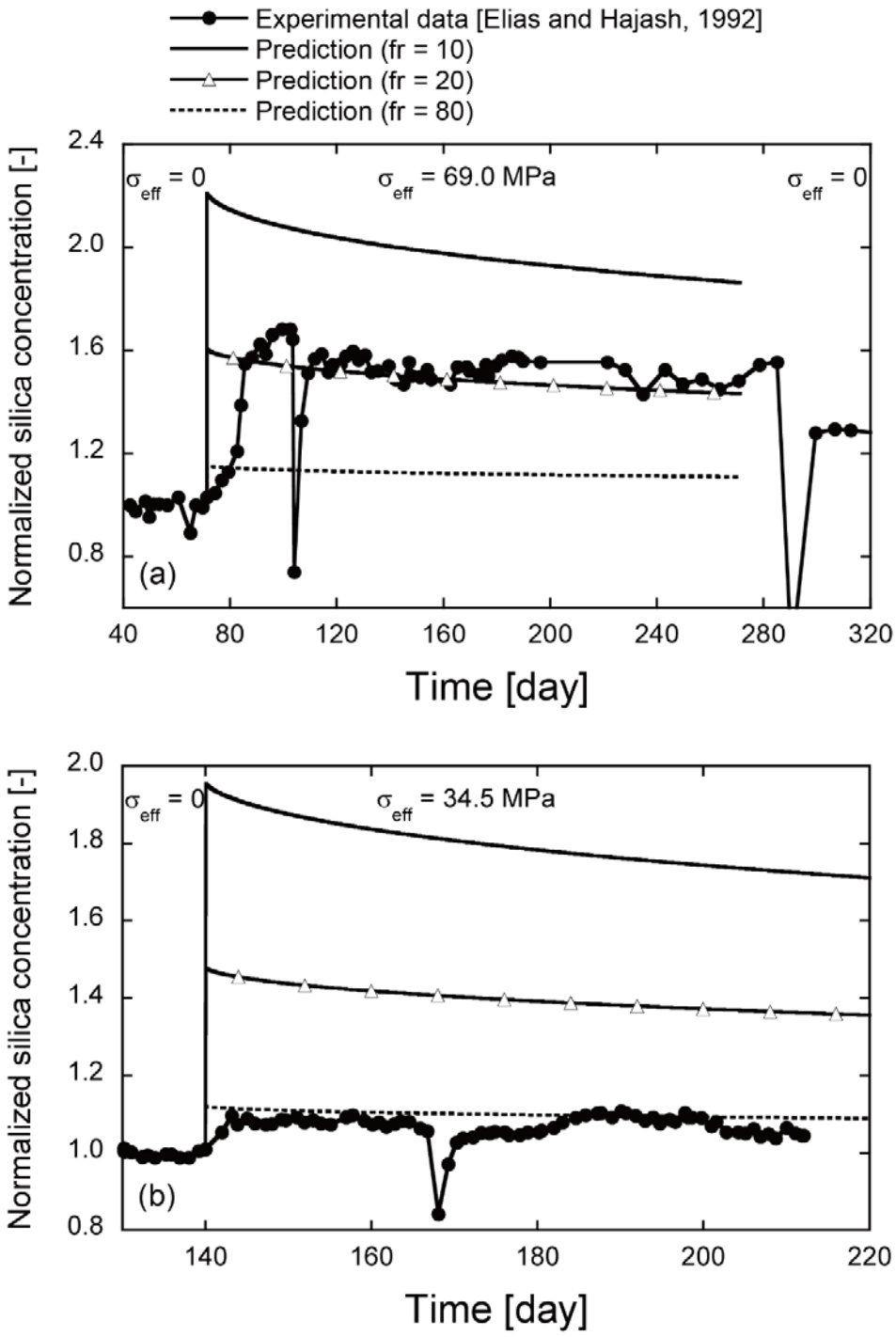

Figure 5. Comparison of silica concentration in pore fluid between experimental data [19] and predictions of the model.

680

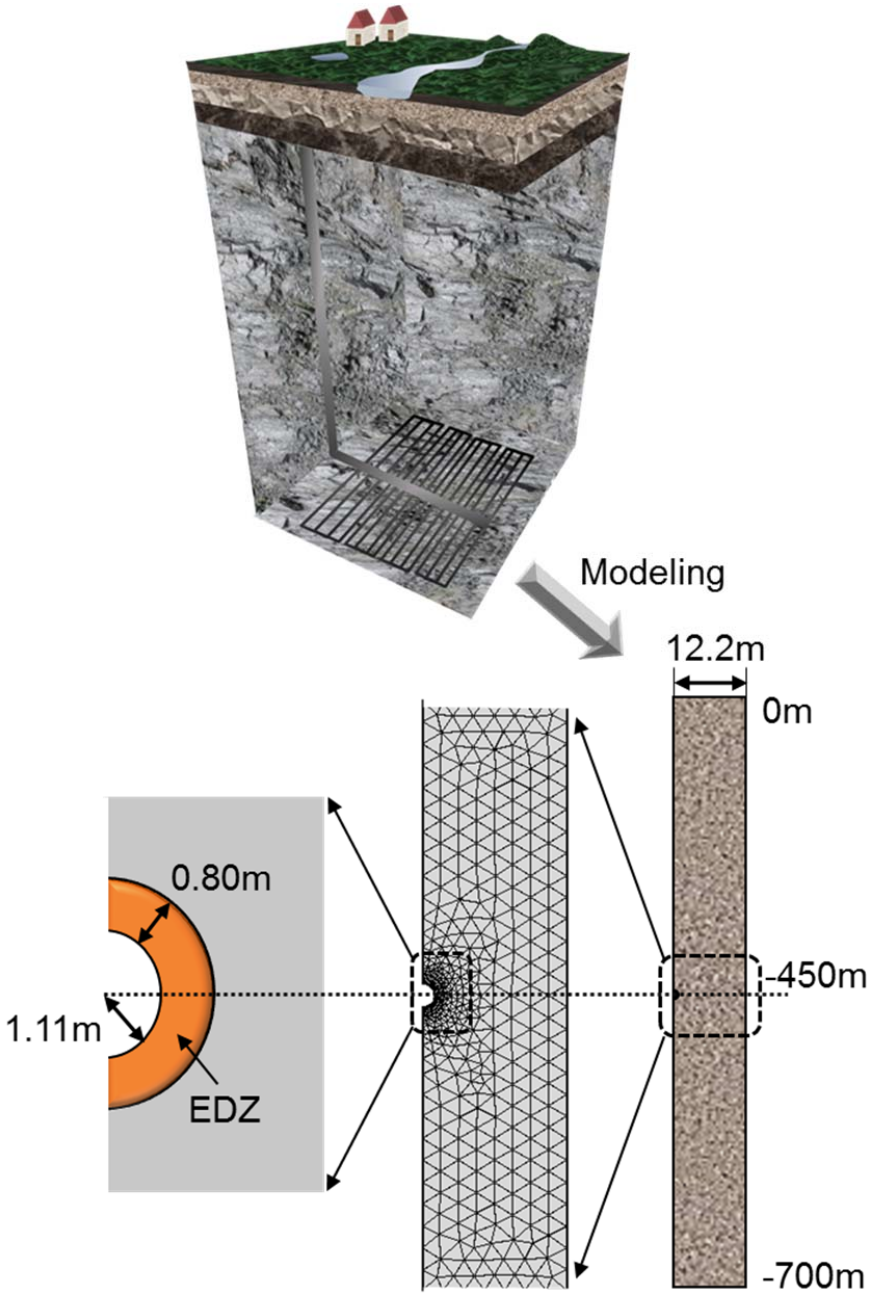

Figure 6. Calculation domain. The calculation domain is a rectangle with vertical and horizontal lengths of 700 and 12.2 m, respectively. The cavity, with a diameter of 2.22 m, is excavated by lateral setting at a depth of 450 m. The EDZ ranges, in the radial direction, from the cavity wall to 0.8 m.

686

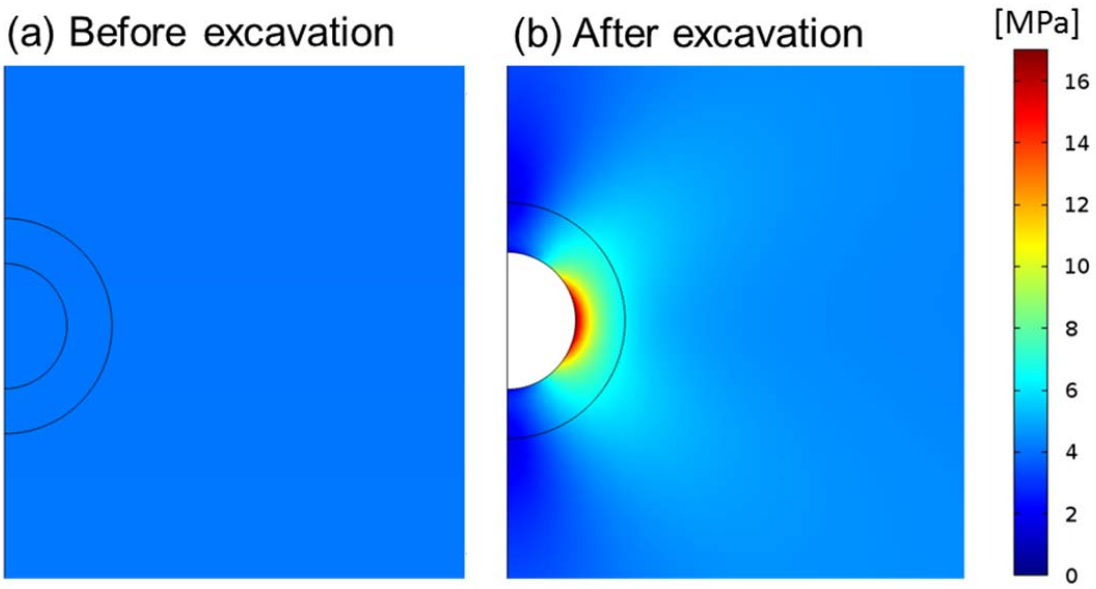

687

688 Figure 7. Distribution of von Mises stress before and after cavity excavation.

689

690

691

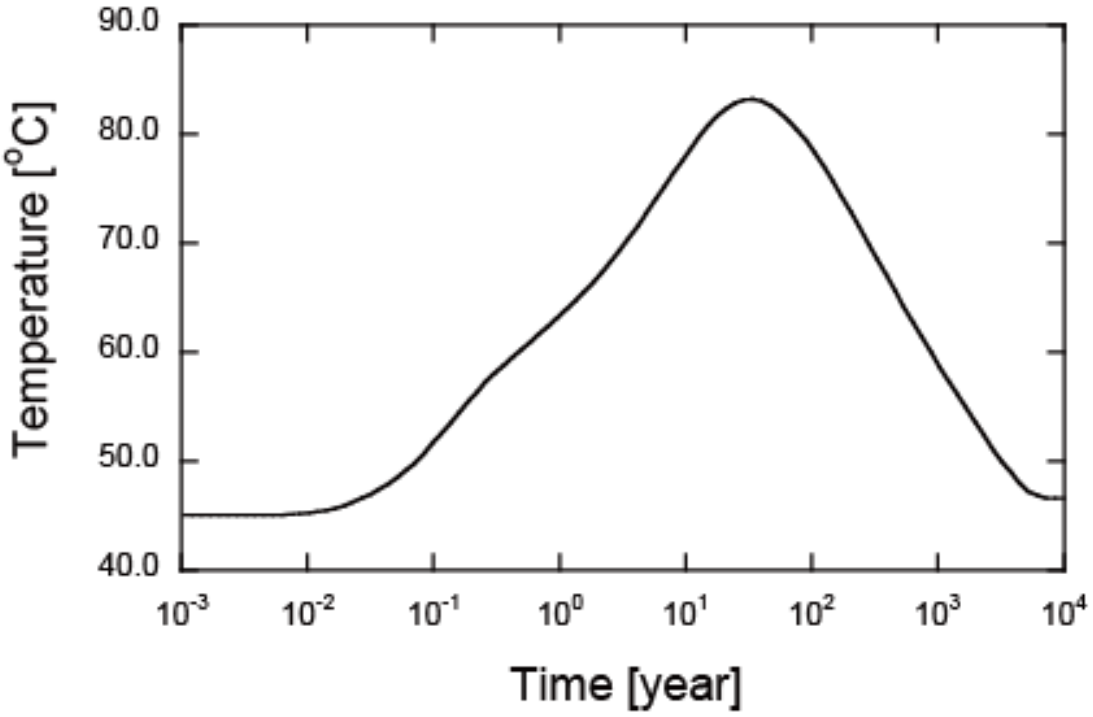

692

693 Figure 8. Temperature change with time that is used as the boundary condition applied on the

694 periphery of the cavity [38].

695

696

697

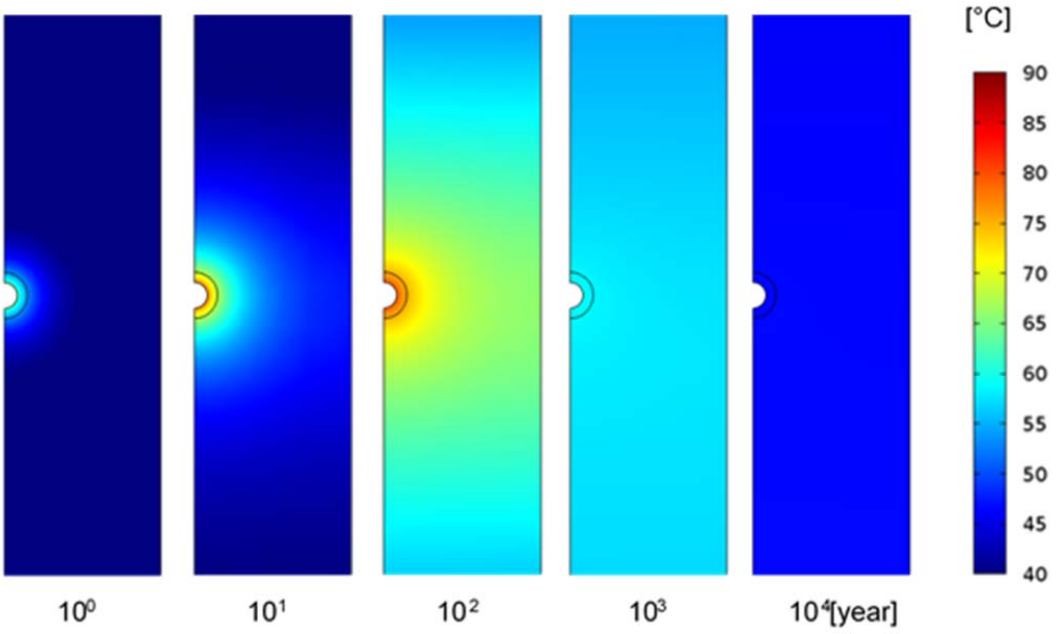

698

699 Figure 9. Change in temperature distribution with time in the range of 10^0 to 10^4 years under the

700 PS condition.

701

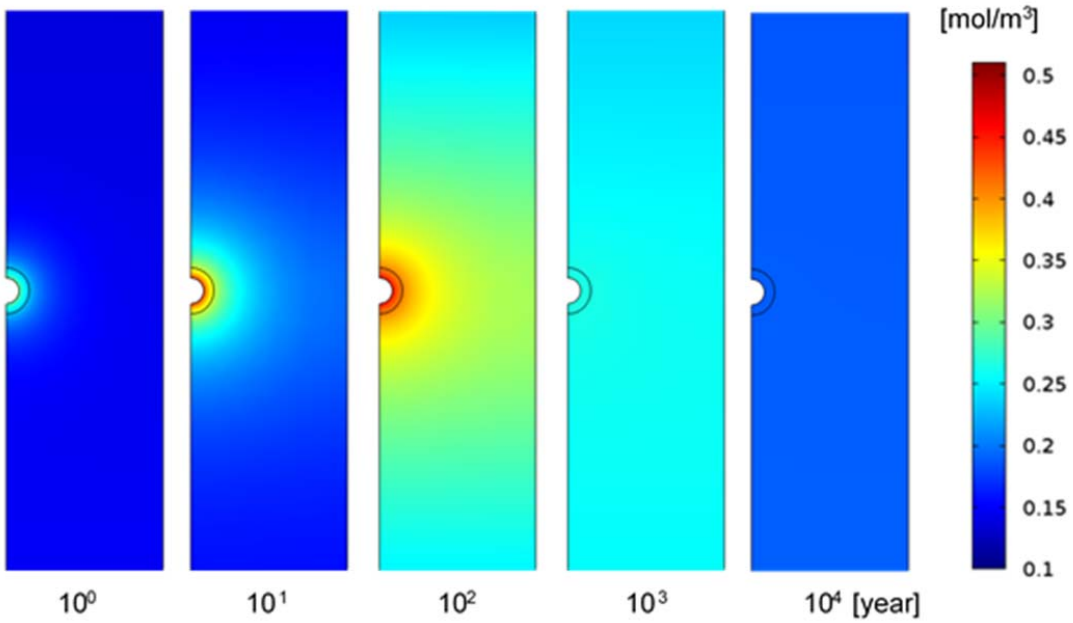

Figure 10. Change in Si concentration distribution with time in the range of 10^0 to 10^4 years under the PS condition.

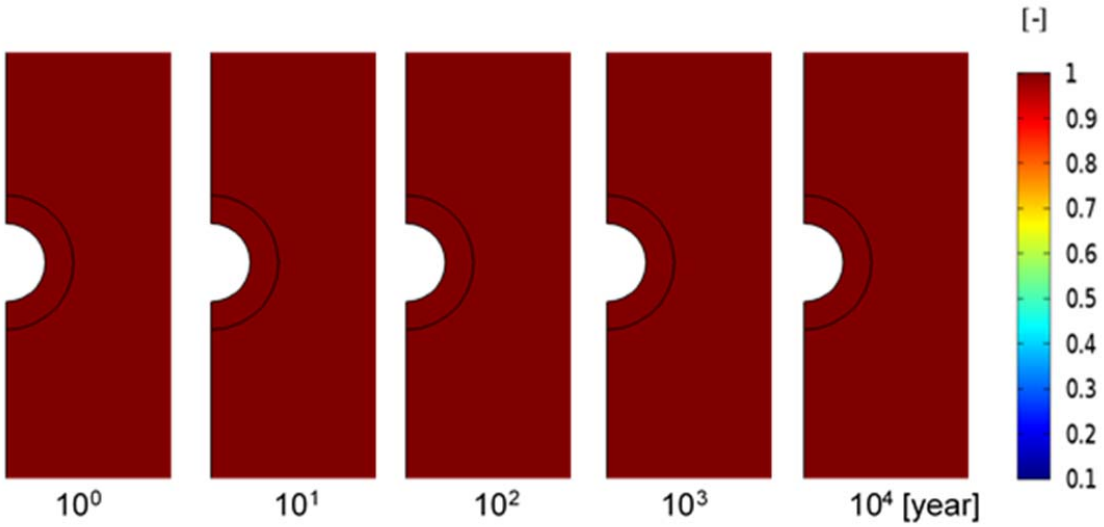

707

708 Figure 11. Change in normalized permeability with time in the range of 10^0 to 10^4 years under the

709 no-PS condition. No permeability change is confirmed.

710

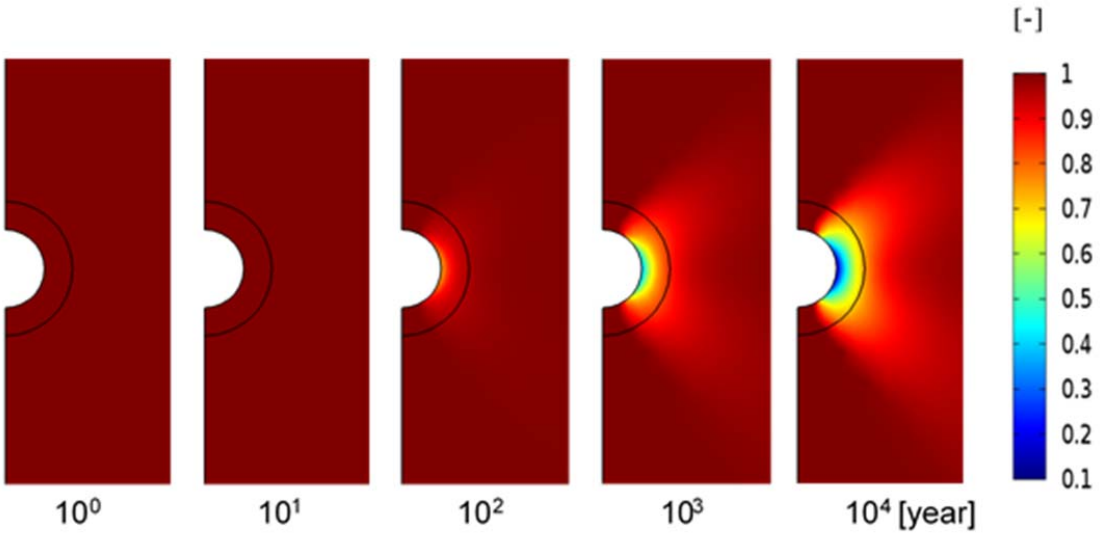

711

712 Figure 12. Change in normalized permeability with time in the range of 10^0 to 10^4 years under the

713 PS condition. The permeability decreases with time. The reduction is especially significant around

714 the periphery of the cavity.

715

716

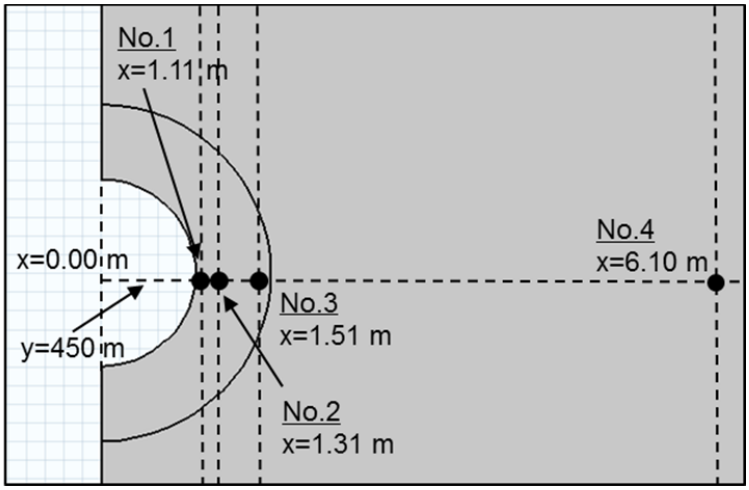

717

718 Figure 13. Specific locations where changes in permeability with time are observed.

719

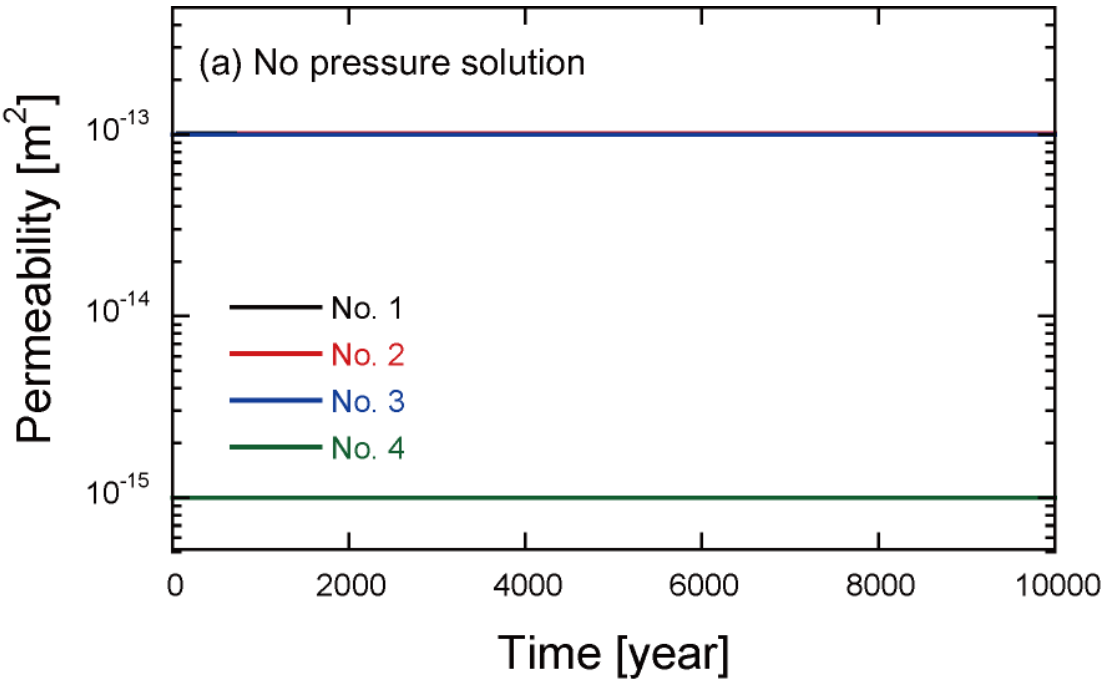

720

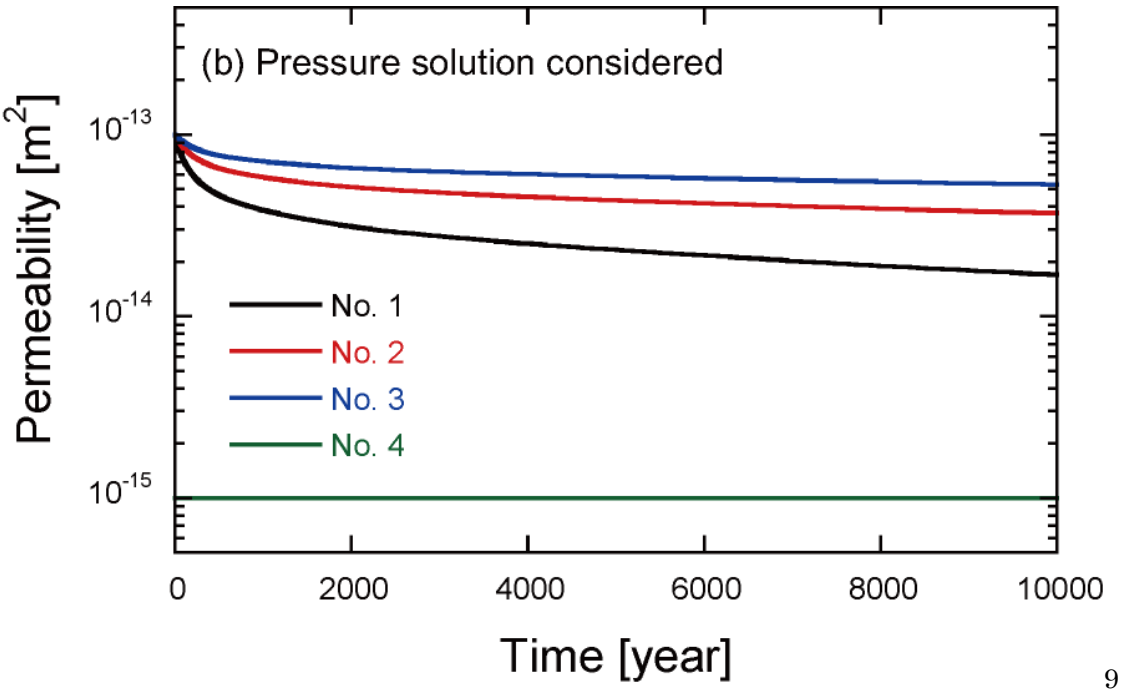

721

9

722 Figure 14. The permeability changes with time at specific locations indicated in Figure 13((a) the

723 no PS condition and (b) the PS condition).

724

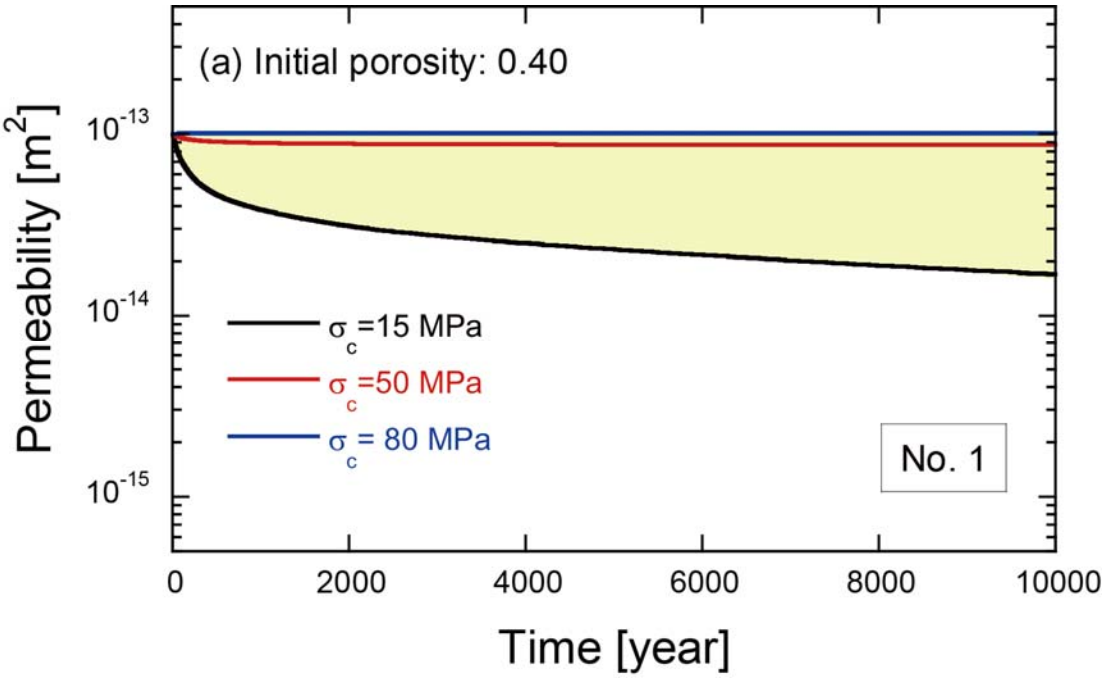

725

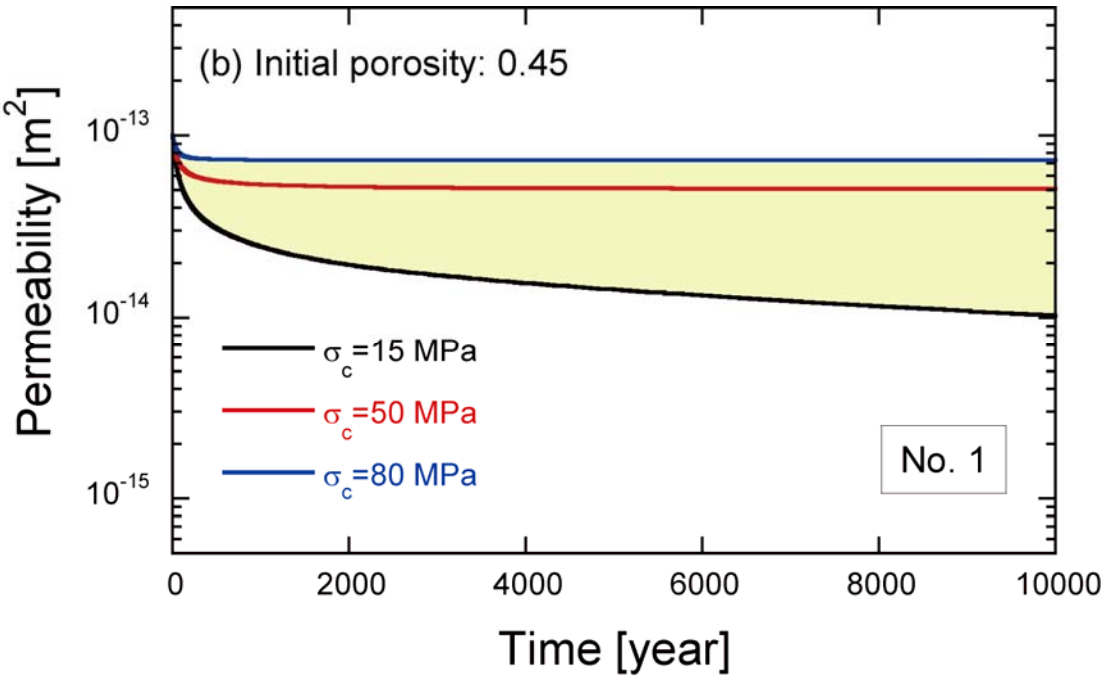

726

727 Figure 15. The permeability changes with time under the PS condition at No. 1, indicated in

728 Figure 13((a) initial porosity of 0.40 and (b) 0.45).

729